



CMS-HIN-24-007

CERN-EP-2025-089
2025/07/21

Exploring small-angle emissions in charm quark jets in proton-proton collisions at $\sqrt{s} = 5.02 \text{ TeV}$

The CMS Collaboration^{*}

Abstract

A measurement of the angular structure of jets containing a prompt D^0 meson and of inclusive jets in proton-proton collisions at the LHC at a center-of-mass energy of 5.02 TeV is presented. The data corresponding to an integrated luminosity of 301 pb^{-1} were collected by the CMS experiment in 2017. Two jet grooming algorithms, late- k_T and soft drop, are used to study the intrajet radiation pattern using iterative Cambridge–Aachen declustering. The splitting-angle distributions of jets with transverse momentum (p_T) of around 100 GeV , obtained with these two algorithms, show that there is a shift of the distribution for jets containing a prompt D^0 meson with respect to inclusive jets. The shift observed in the late- k_T grooming approach is consistent with the dead-cone effect, whereas the shift for splittings selected with the soft-drop algorithm appears to be dominated by gluon splitting to charm quark-antiquark pairs. The measured distributions are corrected to the particle level and can be used to constrain model predictions for the substructure of high- p_T charm quark jets.

Submitted to the Journal of High Energy Physics

1 Introduction

The formation of jets, the highly collimated showers of hadrons produced in high-energy collisions, is a rich multiscale process that probes different emergent phenomena of the strong interaction. Jet substructure techniques allow for an understanding of jet shower formation as a function of momentum scale, providing a view into the building blocks of quantum chromodynamics (QCD). The radiation pattern of jets initiated by gluons or light quarks is governed by the infrared and collinear divergences of QCD [1]. For jets initiated by heavy quarks, such as charm or bottom, these divergences are effectively regularized by the quark mass, which leads to formation of jets where most of their momentum is carried by the heavy quarks. This makes the showering process of heavy-quark jets distinct from those of light-quark or gluon jets. Thus, measurements of heavy-quark jet substructure are needed in order to improve our understanding of the final-state radiation dependence on a mass scale.

The development of iterative jet declustering techniques has enabled the construction of a proxy for the parton branching process. A recent example is the direct observation of the dead-cone effect in proton-proton (pp) collisions at the LHC [2]. The dead-cone effect in QCD is a suppression of gluon emissions off a heavy quark in a cone of angle $\theta_d = m_Q/E_Q$ around the emitting quark [3], where m_Q and E_Q are the mass and energy of the radiating heavy quark. In addition, it has been proposed that the dead cone can potentially be used to understand medium-induced radiation in heavy ion collisions, as it provides an opportunity to study a phase-space region dominated by such emission [4, 5]. Thus, targeted measurements sensitive to the heavy-quark mass and how it affects the jet shower can provide inputs to improve the description of heavy-flavor jet showers. In this analysis, the primary focus is the substructure of charm quark jets, which are identified by the presence of a prompt D^0 meson contained in a jet, referred to as a D^0 jet in the following. Prompt D^0 mesons are those produced directly from the fragmentation of c quark, including c quarks from gluon splittings. Both D^0 and its charge-conjugate state \bar{D}^0 are included in the notation D^0 .

The iterative declustering of a jet allows the kinematic properties and mass effects at the level of an individual emission to be accessed. In an angular-ordered tree, such as the one obtained with the Cambridge–Aachen (CA) pairwise clustering algorithm [6], the splittings that are clustered first have the smallest angular separations, where mass effects are the strongest. The dead-cone angle is different for each splitting, since it depends on the energy of the mother branching.

Using the CA tree, one can map out the kinematics of the intrajet radiation in terms of the Lund jet plane representation [7]. As shown in the right panel of Fig. 1, the Lund jet plane characterizes each individual splitting in terms of the angle θ between the two resulting jets and the relative transverse momentum of the softer subjet with respect to the harder subjet (k_T). The schematic diagram of a splitting in the left panel of Fig. 1 illustrates these two kinematic quantities. This plane enables the visualization of the jet shower in a modular fashion. For instance, one can separate the hadronization and parton showering using a selection on k_T , corresponding to a horizontal line in the Lund jet plane. It also allows for isolating angular regions of interest from one another, in particular the regions where different processes producing prompt D^0 jets are located. Gluon splitting to charm quark-antiquark pairs contributes primarily at large angles θ , hadronization effects contribute primarily to low $k_T < 1 \text{ GeV}$, and the dead-cone effect is located at small angles.

In Ref. [8], two elements were identified as being key for the direct observation of the dead cone:

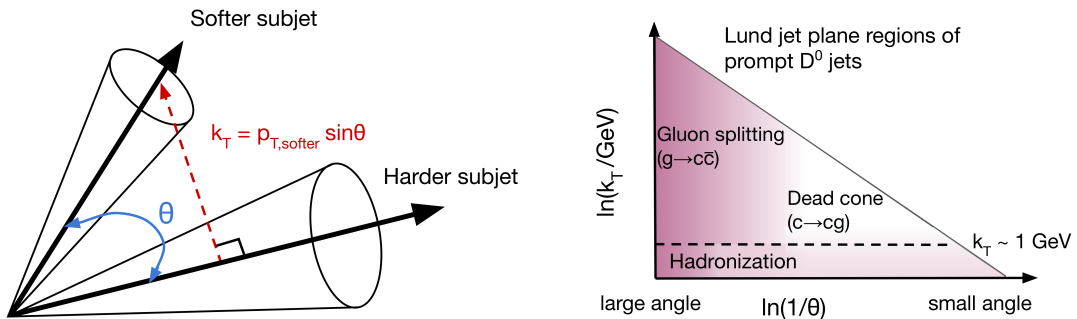


Figure 1: Schematic diagram of two subjets, with their splitting angle θ and the relative transverse momentum k_T of the softer subjet with respect to the harder subjet (left). Different Lund jet plane regions for charm quark jet showers (right), where the vertical axis is the logarithm of the relative momentum k_T of the emission and horizontal axis is the logarithm of the angle between the emission and the emitter θ . The shading represents the density of emissions in the primary Lund jet plane for c quark jets

- Suppression of the decays of the heavy-flavor hadrons that can create additional small-angle splittings in the jet clustering tree, such that the dead cone is filled by them. One way to overcome this issue is to select jets with fully reconstructed heavy-flavor hadrons in them.
- Suppression of hadronization effects that fill the dead cone. This can be achieved by imposing a k_T cutoff on the splittings that is larger than the hadronization scale.

The ALICE Collaboration used the CA jet tree to obtain direct evidence of the dead-cone effect in jets containing a fully reconstructed D^0 meson [2]. Here, an alternative strategy is followed to facilitate comparisons with theoretical calculations, reduce nonperturbative corrections and enable exploration of the QCD dead-cone effect in collisions of heavy ions.

In this analysis, the approach consists in selecting one emission (splitting) per jet, such that the mass effects in heavy-flavor jets are exposed and interpretation of the data for both pp and lead-lead collisions is possible, since this measurement will also serve as a reference for future heavy ion studies. The specific types of emissions are selected by applying a recently proposed grooming algorithm known as “late- k_T ”[4], designed to select hard and collinear emissions. This algorithm selects the last splitting in the CA jet tree with a k_T value larger than a certain threshold of choice, preferably larger than the QCD energy scale $\Lambda_{\text{QCD}} \approx 200 \text{ MeV}$. This procedure enhances sensitivity to charm quark mass effects while strongly suppressing contributions from hadronization and direct gluon splitting into charm quark-antiquark pairs ($g \rightarrow c\bar{c}$).

A modified version of the soft-drop (SD) grooming algorithm [9, 10] with a k_T selection imposed to minimize hadronization effects is also considered. The emissions selected with the SD algorithm are typically found at larger angles than the ones selected with the late- k_T algorithm. Thus, the SD emissions are potentially more sensitive to effects such as $g \rightarrow c\bar{c}$ or the underlying event activity. Comparing the resulting angular distributions obtained with these two algorithms exposes a modification of the angular scale in D^0 jets relative to inclusive jets in a regime of high transverse momentum (p_T) of the jet. In previous measurements of groomed jet substructure of D^0 jets at the LHC [11], the fragmentation of D^0 jets was constrained at lower jet p_T (p_T^{jet}).

In this analysis, the focus is on moderately high- p_T jets with a p_T^{jet} of at least 100 GeV. This min-

imum p_T^{jet} allows for a description in the framework of perturbation theory, while still allowing the sizable impact of the dead-cone effect to be observed. The measurement is performed using pp data at a center-of-mass energy of 5.02 TeV, corresponding to an integrated luminosity of 301 pb^{-1} recorded by the CMS detector in 2017 [12]. In Section 2 the components of the CMS detector are described, as well as the event samples used. Details about the reconstruction of jets and D^0 mesons are presented in Section 3. Section 4 describes the steps in the analysis for both inclusive and prompt D^0 jets, and gives details on the applied corrections. The strategy for the corrections to stable-particle level is discussed in Section 5. The systematic uncertainties in the corrected distributions are described in Section 6. The corrected distributions and their comparison with theoretical predictions are reported in Section 7. A summary of the measurement is presented in Section 8. Tabulated results are provided in the HEPData record for this analysis [13].

2 The CMS detector and event samples

The CMS apparatus [14, 15] is a multipurpose, nearly hermetic detector, designed to trigger on [16, 17] and identify electrons, muons, photons, and (charged and neutral) hadrons [18–20]. A global “particle-flow” (PF) algorithm [21] aims to reconstruct all individual particles in an event, combining information provided by the all-silicon inner tracker and by the crystal electromagnetic and brass-scintillator hadron calorimeters, operating inside a 3.8 T superconducting solenoid, with data from the gas-ionization muon detectors embedded in the flux-return yoke outside the solenoid. The reconstructed particles are used to build τ leptons, jets, and missing p_T [22–24].

The average number of additional interactions per bunch crossing (pileup) during data taking was about two. This low-pileup activity facilitates the use of neutral hadron PF candidates for the substructure measurement, which eases the comparison of the observable to theoretical calculation. The events are required to have a primary vertex reconstructed within 25 cm of the nominal interaction point along the beam direction, and within 2 cm in the transverse plane.

Events of interest are selected using a two-tiered trigger system. The first level, composed of custom hardware processors, uses information from the calorimeters and muon detectors to select events at a rate of around 100 kHz for pp collisions [16]. The second level, known as the high-level trigger, consists of a farm of processors running a version of the full event reconstruction software optimized for fast processing and reduces the event rate to around 1 kHz before data storage [17].

Events with high- p_T jets are collected with a combination of triggers requiring at least one jet with energy above 60 and 80 GeV. The trigger has an efficiency of 92% for offline jets of 80 GeV and of 99% at 100 GeV. The trigger effects are simulated in dedicated Monte Carlo (MC) samples. The difference in the trigger efficiency between data and simulation is accounted for in simulated data as a function of p_T^{jet} .

Simulated events used in this analysis are derived at leading order(LO) with the PYTHIA [25] generator, version 8.230, with the CP5 tune [26], and the HERWIG [27–29] generator, version 7.2.2, with the CH3 tune [30]. These generated samples are passed through a detailed simulation of the CMS detector using GEANT4 [31]. The PYTHIA sample is used to derive MC corrections, while the HERWIG sample is used to assess systematic uncertainties related to the modeling of the parton shower, hadronization, multiparton interactions, and beam-beam remnant interactions. Additional particle-level predictions are compared with the corrected distributions. These predictions are computed at LO with PYTHIA8.303 with the CP5 tune [26, 32, 33]

and HERWIG7 with CH3 tune.

3 Event reconstruction

The jets used in this analysis are clustered from the PF candidates provided by the offline event reconstruction using the anti- k_T algorithm [34, 35] with a distance parameter $R = 0.2$. The choice of using a small R , compared to the typical 0.4, is convenient since this measurement is intended to be a reference for future planned heavy ion collision measurements where small- R will be used to mitigate the impact of uncorrelated background contributions for jet momentum and substructure [36]. Moreover, our focus is the small-angle region of the intrajet radiation pattern, which is the most sensitive to quark mass effects.

The four-momentum of the jet is determined using the vector sum of all particle momenta in the jet. For this analysis, initially selected jets are required to have $80 < p_T^{\text{jet}} < 160 \text{ GeV}$ and pseudorapidity $|\eta| < 1.6$. Our results are reported in the region $100 < p_T^{\text{jet}} < 120 \text{ GeV}$. A fixed p_T^{jet} window is chosen to limit smearing of the dead-cone region, as the effect depends on the p_T^{jet} . A wider range in p_T^{jet} (80–160 GeV) is used for this measurement in order to account for migration when correcting to particle level. The selection of jets at central η is driven by the choice of the D^0 meson candidate selection described in the next paragraph. Jet energy corrections are derived from independent pp simulations along with additional corrections, derived using control samples in data, accounting for the imperfect modeling of the detector response [37]. In addition to the jet energy correction, a correction for the momentum resolution of jets is applied to account for the worse momentum resolution of jets in data compared to simulation. These corrections are derived from dijet balancing studies [23]. To incorporate this effect, a Gaussian smearing is applied to the detector-level p_T^{jet} values in simulation to match the resolution in data.

The D^0 meson candidates are reconstructed by combining pairs of oppositely charged particle tracks with an invariant mass within $\pm 0.2 \text{ GeV}$ of the world-average D^0 meson mass, 1.86 GeV [38]. To compute the D^0 invariant mass, two hypothesis are considered: in the first, one track is assumed to be a pion and the other a kaon; in the second, the particle assignments are swapped. To suppress the contribution of combinatorial background and to improve the momentum and mass resolution, each track is required to have $p_T > 1 \text{ GeV}$ and $|\eta| < 2.4$, and to satisfy a set of track quality selection requirements [20]. The jets that have at least one D^0 candidate at $\eta-\phi$ distance from the jet axis smaller than the jet distance parameter R , are tagged as D^0 -jets. To further suppress the combinatorial background, several topological criteria are applied. The selections are based on the following detector-level variables: the distance between primary and D^0 decay vertices (d_0) normalized by its uncertainty in the direction transverse to the beam, the angle between the total momentum vector of the daughter tracks and the vector connecting the primary and D^0 decay vertices (pointing angle α), the χ^2 probability of D^0 decay vertex fit, and the significance of the distance of the closest approach (DCA) from the total momentum vector to primary vertex. The selection is optimized using binary trees to maximize the statistical significance of the D^0 meson signal [39]. The signal input to this optimization is the generator level D^0 , as given by the simulation. Out of the sample of two million jets with $100 < p_T^{\text{jet}} < 120 \text{ GeV}$, about 25000 of them are found to have at least one D^0 meson candidate in data with the characteristics described here.

Each D^0 meson candidate is selected with $p_T > 4 \text{ GeV}$ and rapidity $|y| < 1.2$. This D^0 p_T requirement is used to suppress the large combinatorial background in D^0 reconstruction in the

heavy ion environment, for which the present measurement is used as a baseline [40]. In addition, it helps to mitigate possible data-to-simulation differences in the reconstruction efficiency of the D^0 meson. Based on MC simulation studies, the D^0 p_T threshold does not introduce a bias in the jet substructure distributions presented in this paper. The same p_T threshold of 4 GeV for the D^0 meson is used for the corrections to the particle level, and no acceptance correction is applied for the meson's p_T , while a correction for the single-particle p_T acceptance is applied to the decay daughters of the D^0 meson.

The observables considered in this analysis are reported at the particle level. To estimate the impact of hadronization effects, the angular distributions at the parton and at stable-hadron levels using events generated with both PYTHIA8 CP5 and HERWIG7 CH3 are computed. For a given MC-generated event, the list of partons and stable hadrons is analyzed simultaneously. At the hadron level, prompt D^0 jets are selected with the same kinematic selection requirements on the jets and the D^0 meson in the jet, and with the same grooming algorithm parameters as in the rest of the analysis. At the parton level, jets are required to have a charm quark as a constituent (since there is no D^0 meson formed yet), and the CA reclustering is performed over the list of partons as provided by the respective MC generator. Only parton- and hadron-level jets that are matched geometrically (closest in η - ϕ space, where ϕ is azimuthal angle) are used for this comparison. Hadronization effects are quantified through the bin-by-bin difference between the hadron-level jet substructure observable and the substructure of the matched parton-level jet. Hadronization effects are of the order of 10% across the entire angular range for both late- k_T and SD grooming, demonstrating the resilience of these observables to hadronization effects.

4 Analysis method

This analysis reports the angular distribution of the intrajet emissions in two different regions of the Lund plane for jets containing a prompt D^0 meson and inclusive jets, as selected by two grooming algorithms, the late- k_T and a modified version of the SD algorithm, as described next.

First, the anti- k_T jets [34, 35] are reclustered using the CA algorithm, which is a pairwise clustering algorithm that clusters particles (and subjets thereafter) that are closer in rapidity and azimuth, imposing angular ordering [6, 41]. The PF candidates with $p_T > 1$ GeV of the original anti- k_T jet are used for the CA reclustering step, which includes neutral and charged PF candidates. This p_T threshold is required to ensure high tracking efficiency and reduce data-to-simulation differences.

Then, the CA pairwise clustering history is followed in reverse. Starting with the reclustered jet, the last step of the CA clustering is undone, such that the original jet is “declustered” into the two subjets of the previous clustering step. This procedure is performed iteratively, declustering the harder subjet at each step of the iteration. Jet grooming consists of selecting a specific pair of subjets from this iterative CA declustering procedure.

The late- k_T grooming algorithm selects the last pair of subjets that satisfies the $k_T > 1$ GeV selection, where $k_T = \theta p_T^{\text{sub}}$, p_T^{sub} is the transverse momentum of the subleading subjet at the respective declustering step, and θ the distance in y - ϕ between the harder and softer subjets in the declustering procedure, as shown in Figure 1 left. The late- k_T algorithm scans the region of collinear and hard emissions in the Lund jet plane.

The SD grooming algorithm selects the first pair of CA subjets that satisfies the condition $z > z_{\text{cut}} \theta^\beta$. Here, z corresponds to the momentum fraction $z = p_T^{\text{sub}} / (p_T^{\text{sub}} + p_T^{\text{lead}})$ where p_T^{lead} (p_T^{sub}) is the momentum of the harder (softer) subjet in the declustering step, z_{cut} and β are

SD tunable parameters. In the modified version of the SD algorithm that used in this analysis, the first splitting that satisfies the two requirements is selected: $z > z_{\text{cut}}\theta^{\beta}$ and $k_T > 1 \text{ GeV}$. The parameters are set to $z_{\text{cut}} = 0.1$ and $\beta = 0$, which facilitates the comparison with theoretical calculations [42]. The additional k_T requirement is applied to reduce the sensitivity to hadronization effects at small angles, thereby improving the correspondence between the parton- and hadron-level predictions.

For D^0 jets using both grooming algorithms, it is required that the D^0 meson is a constituent of the harder of the two selected subjets.

The angles between the softer and harder subjets selected by the late- k_T or the modified SD grooming algorithm, denoted by θ_1 or θ_{SD} , respectively, are the main observables reported in this measurement. The present analysis reports such splitting angle distributions for prompt D^0 jets and for inclusive jets. The inclusive jet sample is dominated by light-quark and gluon jets.

The analysis workflow for D^0 jets can be summarized by the following steps. The D^0 meson candidates are reconstructed, as described previously. The two charged-particle track daughter candidates are combined to form the four-momentum of the D^0 meson candidate. This D^0 meson candidate replaces the two daughters, which are removed from the list of particles that are used as input for the jet clustering. The jet substructure observables are computed using the jets that contain at least one D^0 meson candidate as a constituent. The D^0 meson yield in each p_T^{jet} and θ_1 (θ_{SD}) bin is extracted with a binned maximum likelihood fit to the invariant mass distributions of the D^0 candidate in the range $1.7\text{--}2.0 \text{ GeV}$. The signal shape is modeled as the sum of two Gaussian functions with the same mean but different widths. The combinatorial background originating from random pairs of tracks is modeled with a third-order polynomial function. An additional Gaussian function with a larger width is used to model the invariant mass distribution of D^0 meson candidates that result from the incorrect mass assignment for the pion and kaon tracks. Backgrounds from decays $D^0 \rightarrow K^+K^-$ and $D^0 \rightarrow \pi^+\pi^-$ are modeled with Crystal Ball functions. An example of such fit is shown in the Fig. 2 (left).

It is likely that the clustering of a pair of particles with a combined $p_T > 4 \text{ GeV}$ and with an invariant mass compatible with the D^0 meson could modify the jet substructure distribution so that it mimics the dead-cone effect. In order to test this, a check is performed using the D^0 candidates from low- and high-mass sidebands of the invariant mass distribution ($0.07 < |m_{\pi K} - m_{PDG}^D| < 0.12 \text{ GeV}$). The substructure distribution of sideband- D^0 jets is found to be compatible with the inclusive jet baseline, showing that there are no significant kinematical biases, as seen in the right plot in Fig. 2.

The yield of D^0 mesons extracted from the invariant mass fits includes both the prompt and nonprompt components. Nonprompt D^0 mesons are those D^0 mesons that do not originate from the fragmentation of a charm quark but that come from decays of bottom hadrons. In this case, the reconstructed jet will contain the D^0 meson and other particles from the b hadron decay as constituents. These other decay products may create extra splittings in the CA declustering, leading to contamination in the collinear region of interest.

The prompt D^0 contribution is extracted from the DCA significance distribution which shows good separation from the nonprompt component. Figure 3 (left) shows the detector-level DCA significance distribution fitted with a linear combination of prompt and nonprompt D^0 DCA templates obtained with PYTHIA8 simulated events. The data distribution is obtained by extracting signal D^0 yields using the invariant mass fits in bins of DCA significance. The nonprompt and prompt D^0 meson templates derived from HERWIG7 CH3 simulated samples are

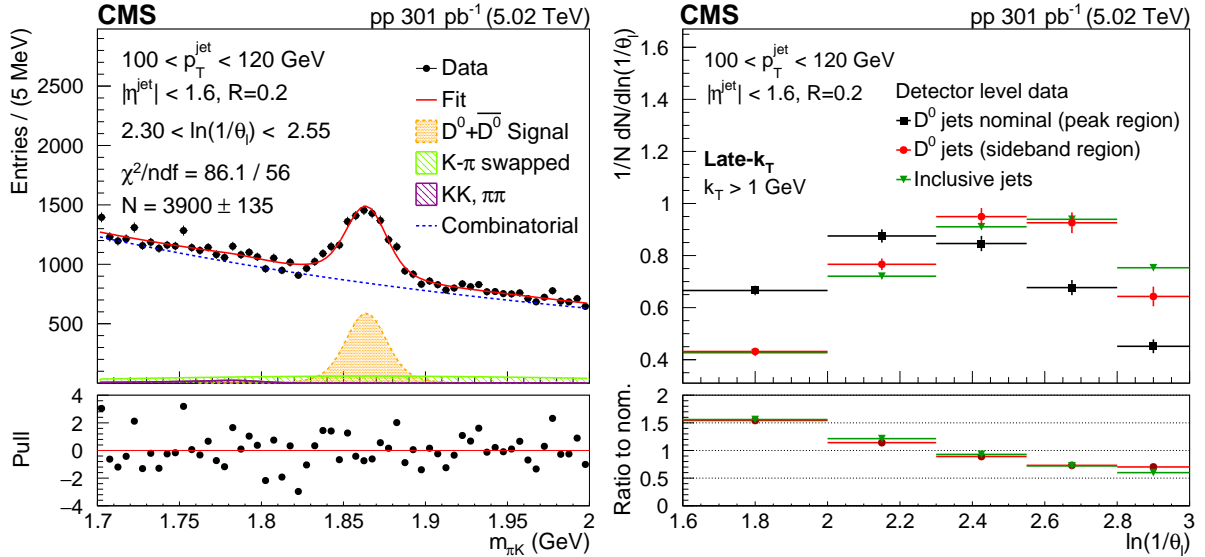


Figure 2: Invariant mass distribution of particle pairs for D^0 jet candidates and fits for late- k_T for splitting angle and jet momentum in the range: $2.3 < \theta_l < 2.55$ and $100 < p_T^{\text{jet}} < 120 \text{ GeV}$ (left). Comparison of the $\ln(1/\theta_l)$ distributions for invariant mass of the track pairs in the resonance region (black rectangles), in the mass sideband region $0.07 < |m_{\pi K} - m_{PDG}^D| < 0.12 \text{ GeV}$ (red circles) and for inclusive jet data (green triangles)(right). In the lower panel, a ratio to nominal signal is shown. The error bands represent the statistical uncertainties. The ndf is number of degree of freedom.

compatible in shape with the ones derived from PYTHIA8. Figure 3 (right) shows the D^0 jet substructure distribution and nonprompt D^0 meson contribution obtained with fits in bins of DCA, splitting angle, and p_T^{jet} . The nonprompt D^0 meson contribution is found to be around 15%. The nonprompt D^0 subtraction causes a reduction of the uncorrected yield and a change in the shape of the substructure distribution.

To account for bin migration effects due to detector resolution, the prompt D^0 jet substructure is corrected to the particle level. This correction is a two-dimensional unfolding where p_T^{jet} and the splitting angle of interest (either θ_l or θ_{SD}) are unfolded simultaneously. The number of jets that do not satisfy the grooming criteria is tracked through the analysis so that all possible migrations are taken into account. Among inclusive jets around 25% fail grooming criteria, while this fraction is 30-40% for D^0 jets. The same p_T selections on particles are applied at the detector and particle level, including the 4 GeV cutoff on the D^0 meson p_T . Finally, the unfolded result is corrected by the selection, acceptance, and reconstruction efficiency of the prompt D^0 mesons. The efficiency correction factor is of the order of 50% and has a weak dependence on the splitting angle. This emphasizes the fact that decay properties on which our D^0 selection is based are uncorrelated with the jet substructure. The procedure is detailed in the next section. To reduce data-to-simulation differences in the jet energy calibration for prompt D^0 jets, the ratio distribution of the D^0 and jet momentum in the detector-level simulation is reweighted to match the data distribution.

5 Corrections to the particle level

The measured detector-level distributions are corrected to the stable-particle level using corrections derived from the simulation. The particle level is defined by the set of particles that have

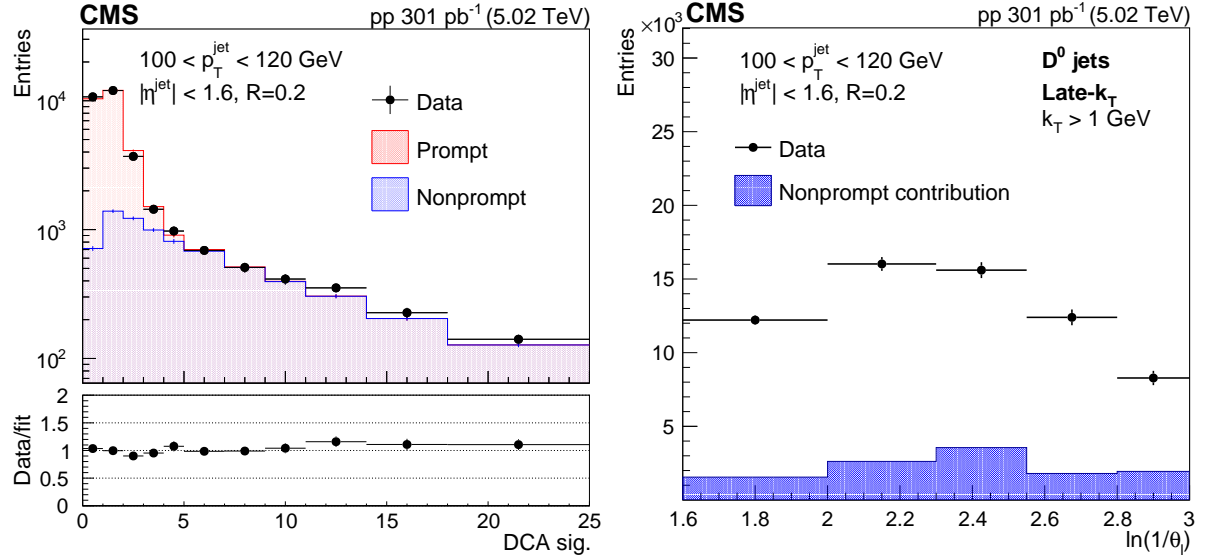


Figure 3: Detector-level DCA significance distribution in data fitted with PYTHIA8 CP5 templates for prompt and nonprompt D⁰ mesons contained in jets (left). In the lower panel, the ratio between the data and the fit values is presented. Measured D⁰ meson yield (black circles) and nonprompt D⁰ meson contribution (filled histogram) as functions of the late- k_T splitting angle θ_l (right).

a lifetime longer than 10^{-8} s as given by the MC event generator. For the simulated prompt D⁰ jet signal events, the D⁰ mesons replace the kaon and pion daughters before the jet reclustering, analogous to what is done at the detector level. The D⁰ meson replacement at the particle level uses generator-level information for the mother-daughter association. For the inclusive jet corrections, such a replacement is not performed. First, a set of bin-by-bin corrections is applied to the detector-level distribution to account for the background (purity corrections). In this measurement, the background consists of detector-level emissions that are not paired with particle-level emissions. Then, to correct for bin-to-bin migrations due to detector effects, a two-dimensional unfolding of p_T^{jet} and the angular variable of interest is applied. Unfolding is performed in three bins of p_T^{jet} , where the middle bin is reported and the surrounding bins are used to allow migrations. After the correction for bin-to-bin migration effects, a set of bin-by-bin corrections to account for particle-level emissions that are not reconstructed at the detector level (efficiency corrections) is applied. At the particle and detector levels, jets are clustered with a $p_T > 1$ GeV requirement on the particles used for the jet CA reclustering (with the exception of the D⁰ meson in the case of the D⁰ jet analysis, where an additional selection of $D^0 p_T > 4$ GeV is required). The particle-level distribution shares the same binning as the detector-level distribution, and in addition has overflow and underflow bin to account for phase-space migrations in the unfolding procedure.

To derive the corrections, a mapping between the detector- and particle-level emissions is necessary. If the particle- and detector-level jets satisfy the grooming criteria, the splittings selected at the particle and detector levels are required to be, in addition, the closest in proximity among all the primary emissions in the detector- and particle-level CA trees. The cases where the mapping criteria are not satisfied are accounted for via purity and efficiency corrections.

For each of the grooming algorithm, a two-dimensional unfolding is performed to correct for the bin-to-bin migrations caused by the detector effects. The dimensions that are considered in the correction are the anti- k_T p_T^{jet} and the splitting angle (θ_l or θ_{SD}). Since unfolding with

direct matrix inversion yields large bin-to-bin oscillations in the unfolded distributions, the regularized matrix inversion using iterative D’Agostini unfolding with early stopping [43] is performed. Its implementation in the ROOUNFOLD package [44] is used.

The number of iterations plays the role of the regularization parameter in iterative D’Agostini unfolding. A value for the number of iterations must be chosen. In this analysis, the number of iterations is chosen based on χ^2 goodness-of-fit tests at the detector level. At each iteration of D’Agostini unfolding performed using PYTHIA8 CP5, the unfolded distribution is mapped back to the detector level by matrix multiplication using the same migration matrix. This process is referred to as “forward folding”, and the detector-level distribution obtained after matrix multiplication as the “forward-folded distribution.” To quantify the compatibility between the forward-folded distribution and the input-measured distribution, the χ^2 of the forward-folded distribution and the measured detector-level distribution are calculated at a given iteration. By construction of the D’Agostini unfolding algorithm, the agreement between the input distribution and the forward-folded distributions improves monotonically at each iteration. To avoid overfitting the unfolded distribution to the statistical fluctuations present in the measured distributions, the unfolding algorithm is stopped at the iteration at which the corresponding p -value reaches a plateau.

The nominal set of corrections is derived using the sample of PYTHIA8 CP5 simulated events. The sample of HERWIG7 CH3 simulated events is used to estimate biases in the unfolding corrections and to compute the systematic uncertainties associated with the model dependence of the corrections, as described in Section 6.

6 Systematic uncertainties

The experimental uncertainties are propagated by repeating the unfolding procedure with variations of the response matrix, prior distribution, purity, and efficiency corrections. The following systematic uncertainties are considered:

Jet energy scale and resolution: The jet energy scale uncertainty is propagated through the unfolding by shifting the p_T^{jet} at the detector level in the simulation according to the η – p_T dependent jet energy scale uncertainties (3–4%) [23]. This uncertainty has an effect through the $80 < p_T^{\text{jet}} < 160 \text{ GeV}$ selection requirement. The uncertainties in the jet energy resolution measurement [23] is also considered. The p_T^{jet} is further smeared at detector level in simulation to better reproduce the jet energy resolution measured in data [23]. Such a smearing procedure comes with an associated systematic uncertainty (2–4%), which is propagated through the unfolding procedure.

PF candidate energy scales: For a given anti- k_T jet, the four-momenta of the jet constituents are shifted by 1% for charged particles, 5% for neutral hadrons, and 3% for photons [21, 23, 45]. With these variations, the impact of the individual calibration of PF candidate is estimated. The variations are done independently for each PF candidate type, treating the up and down variations as uncorrelated. This corresponds to six different variations.

Tracking efficiency: To account for the mismodeling of track reconstruction in the simulation we propagate the track reconstruction efficiency uncertainty through the unfolding procedure. This is done by randomly removing 3% of the tracks in the simulation. This value covers mismodeling of the tracking reconstruction efficiency in the jet core [23]. The tracking efficiency has two effects in this analysis. One of them is at the substructure level, whereas the other has to do with the reconstruction of the D^0 meson candidate. The D^0 meson reconstruction relies

on charge-particle tracks and the removal of 3% of the tracks is done before the D^0 meson candidate reconstruction. The jet substructure is calculated using all PF candidate species. Rather than losing the PF candidate, as it would happen in a charged-only jet substructure measurement, we assume that the charged hadron is reconstructed instead as a neutral hadron, and its energy is smeared by 10% due to the hadronic calorimeter resolution. The tracking efficiency uncertainty is propagated through the whole chain of corrections in a correlated way, affecting the D^0 meson reconstruction efficiency, the response matrix through the energy resmearing of the charged-particle PF candidates that are “lost” in the reconstruction from this variation, as well as the MC-based template fits that are used for the nonprompt D^0 meson background subtraction. The dominant effect is the reduction of the D^0 reconstruction efficiency. This systematic uncertainty is symmetrized bin-by-bin for both D^0 and inclusive jet substructure distributions.

Physics model uncertainty: The choice of the physics model impacts the unfolding corrections of the measured observable via the description of the jet showering pattern, which changes the detector response at the subjet level, as well as the prior spectrum used for regularization. The model uncertainty is constructed by using HERWIG7 CH3 generated events instead of PYTHIA8 CP5 for the prior spectrum, the migration matrix, and the matching purity and efficiency.

Response matrix statistical uncertainties: The statistical uncertainties of the simulated sample that is used to derive the migration matrix are propagated through the unfolding procedure, which results in a contribution to the covariance matrix.

Signal extraction and background modeling: The D^0 meson yield extraction is performed using a triple Gaussian function, instead of the nominal double Gaussian function used by default. The variation is made to take into account possible deviations in the shape for the nominal configuration. The uncertainty associated with the modeling of the combinatorial background is estimated by using an exponential function and a second-order polynomial instead of the nominal approach of using a third-order polynomial.

Prompt D^0 meson fraction: Nominally, the prompt D^0 meson fraction is determined via template fits of prompt and nonprompt D^0 meson production using the DCA significance distribution. To avoid possible detector simulation biases on the DCA significance variable, we use an alternative method for the prompt D^0 meson extraction based only on the DCA distribution. A correction to the detector-level DCA in simulation is applied in order to improve the DCA resolution, following the method described in Ref. [46]. The template fits based on the DCA distribution are repeated after this correction, leading to the uncertainty in the prompt D^0 meson fraction with respect to the nominal DCA significance method.

Regularization bias: The optimal number of iterations in the D’Agostini method depends on the initial particle-level spectrum. To gauge the dependence on the initial spectrum, the unfolding of the data using a PYTHIA8 CP5 response is repeated for the optimal number of iterations found when unfolding data with a HERWIG7 CH3 response.

Fit function modeling of the trigger scale factor: The trigger efficiencies in data and simulation are fitted with an error function parametrization instead of the nominal sigmoid function used as default. The correction chain is repeated with this modification, and the difference relative to the nominal choice is used to quantify this systematic uncertainty.

The resulting relative systematic uncertainties on the normalized jet substructure distributions are summarized in Table 1. The dominant systematic uncertainties are the jet energy scale, physics model and PF scale uncertainties.

distribution to that of inclusive jet. The D^0 jet angular distributions are effectively “shifted” towards larger splitting angles relative to the inclusive jet distributions. Since dead cone suppresses collinear radiation, the observed shift of emissions towards larger angles is consistent with expectations.

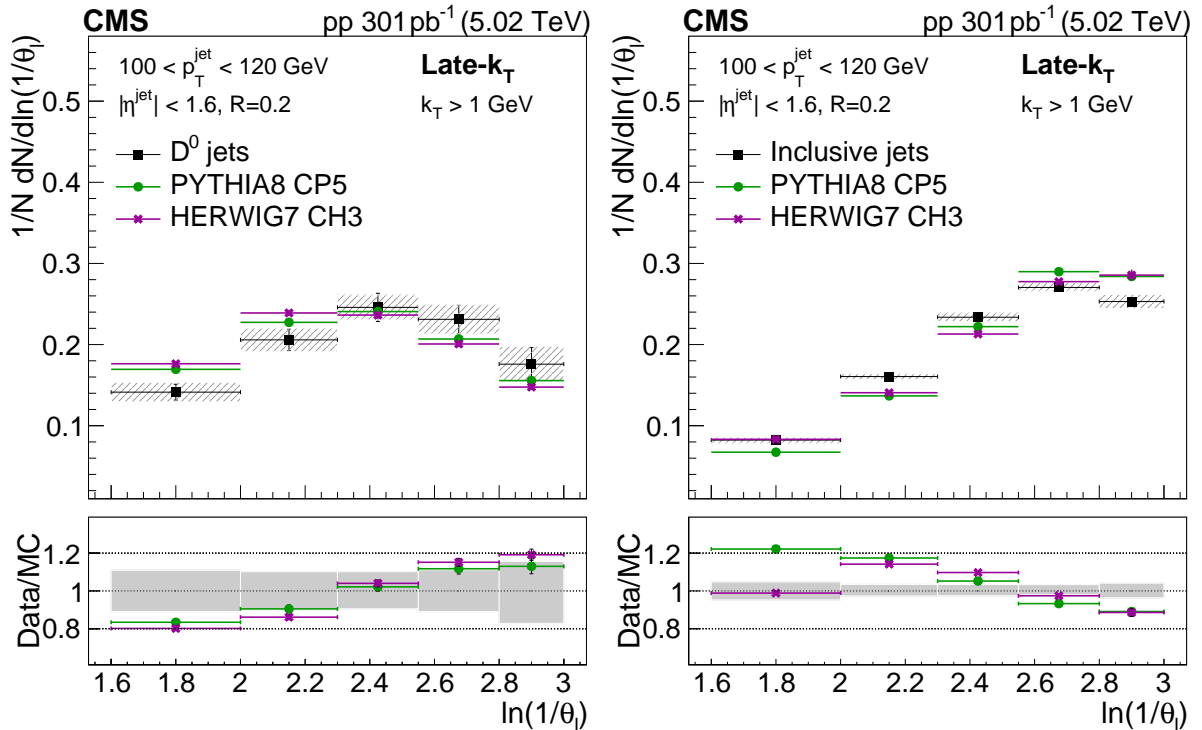


Figure 4: The unfolded late- k_T angular distribution for prompt D^0 jets (left) and inclusive jets (right) compared to the predictions from PYTHIA8 CP5 and HERWIG7 CH3. The error bands in the upper panel represent the total systematical uncertainty, whereas the vertical bars represent the statistical uncertainties. In the lower panel, the error band in the ratio plot represents the total experimental uncertainty in the measurement.

Prompt D^0 mesons from $g \rightarrow c\bar{c}$ are considered as part of the signal in the analysis. Their impact on the ratio of the distributions of prompt D^0 jets to inclusive jets is studied in PYTHIA8 CP5 and HERWIG7 CH3 simulated events and shown in Fig. 7. In both MC generators used in this analysis, events can be generated without gluon splitting to heavy-flavor quark-antiquark pairs, which can be used to understand their contribution to the substructure of prompt D^0 jets. In Fig. 7, gluon splitting is deactivated only for the prompt D^0 jet distributions. The ratio of D^0 jet to inclusive jet is better described by events simulated with the HERWIG7 CH3, which is mostly because HERWIG7 CH3 describes the inclusive jet distribution better than PYTHIA8 CP5. For the late- k_T algorithm, the gluon splitting contribution is negligible and has an effect mostly at large angles. For the SD algorithm, the gluon splitting direct contribution is stronger and plays a role in the observed shift between the D^0 jet and inclusive jet distributions. This is consistent with the expectation that gluon splitting contributes predominantly at large splitting angles. The emissions found with SD grooming tend to be at larger angles than the ones found by the late- k_T algorithm, so the contribution of gluon splittings is enhanced for the SD algorithm because of that.

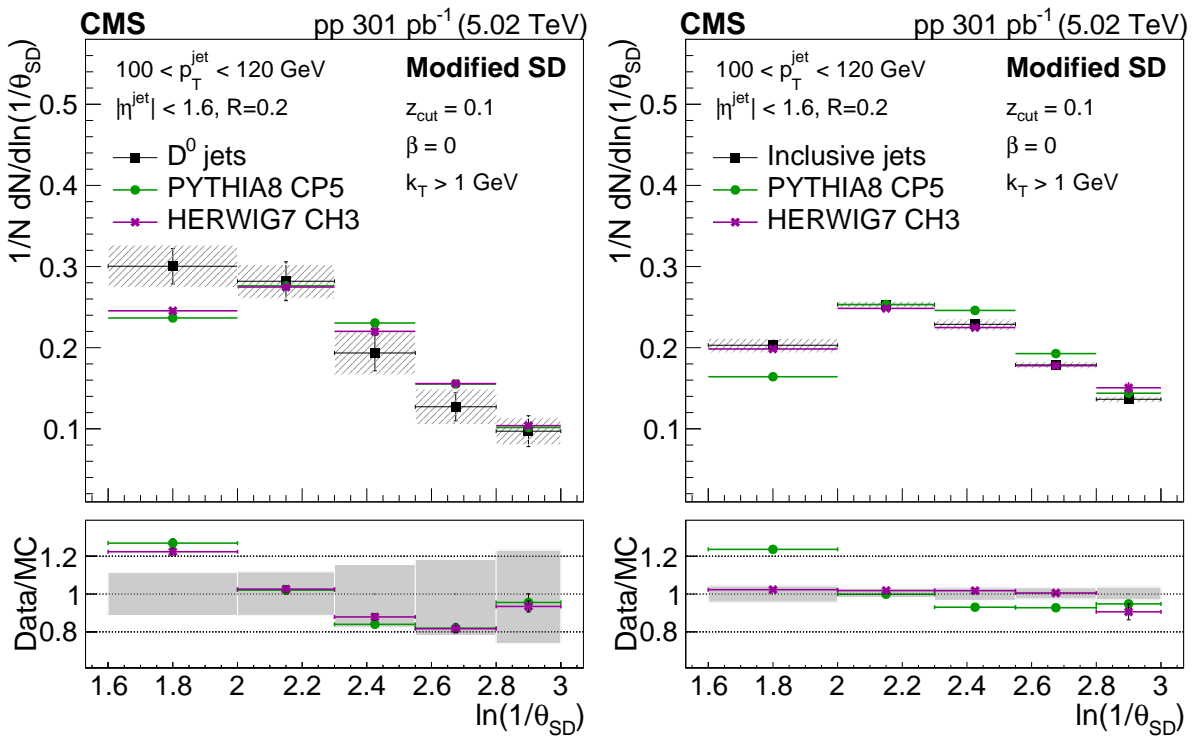


Figure 5: The unfolded SD angular distribution for prompt D^0 jets (left) and inclusive jets (right) compared with predictions from PYTHIA8 CP5 and HERWIG7 CH3. The error bands in the upper panel represent the total systematical uncertainty, whereas the vertical bars represent the statistical uncertainties. In the lower panel, the error band in the ratio plot represents the total experimental uncertainty in the measurement.

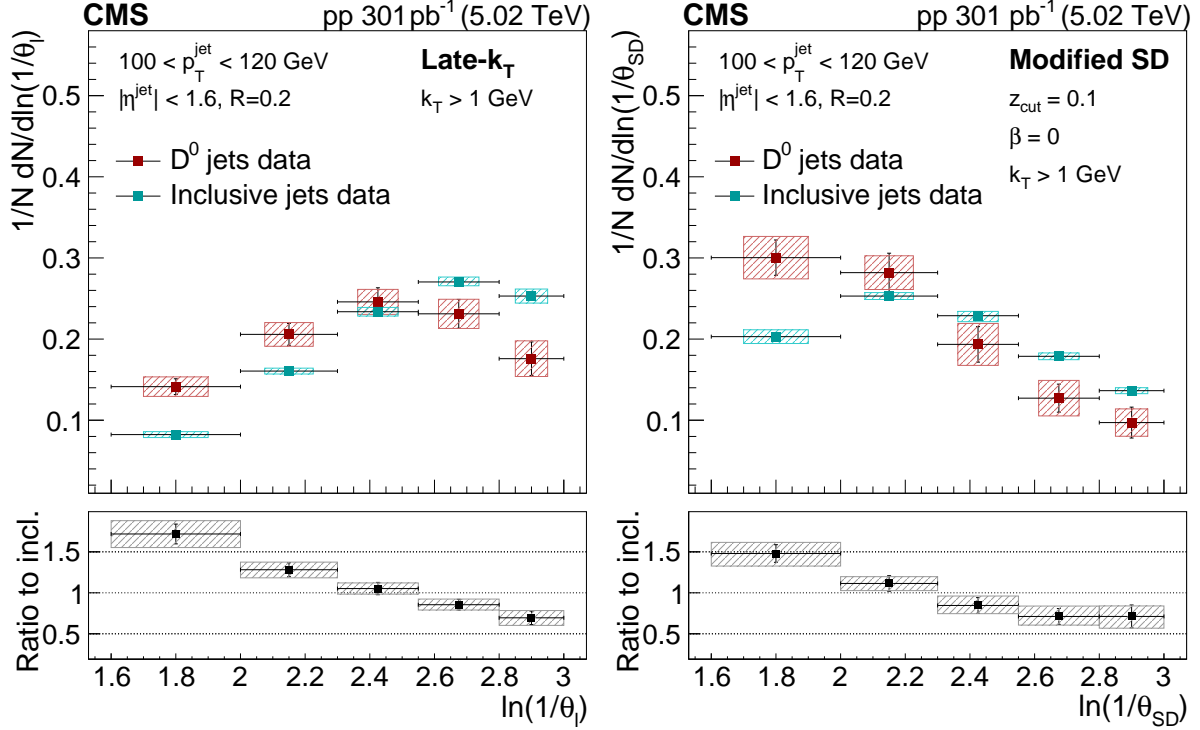


Figure 6: The late- k_T (left) and modified SD (right) angular distribution for prompt D^0 jets and inclusive jets. The ratio to the inclusive jets is shown in the lower panels. The error boxes represents the total systematic uncertainty, whereas the vertical bars represent the statistical uncertainty.

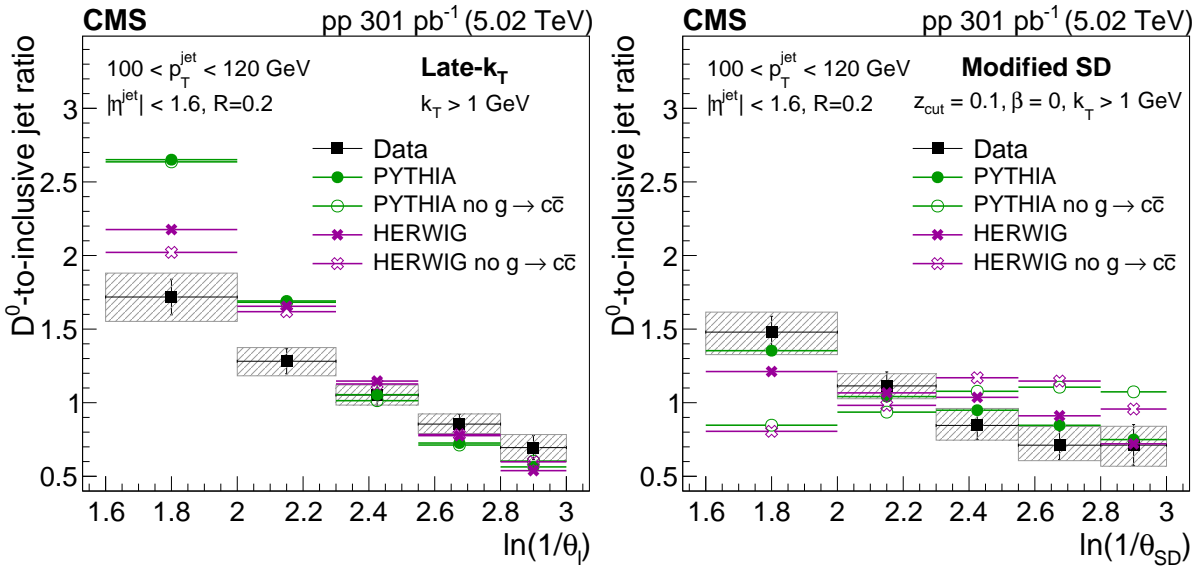


Figure 7: The ratio of the late- k_T (left) and SD (right) angle distributions for prompt D^0 jets to inclusive jets. The data are compared to PYTHIA8 CP5 and HERWIG7 CH3 predictions with and without $g \rightarrow c\bar{c}$. The error boxes represents the total systematic uncertainty, whereas the vertical bars represent the statistical uncertainties.

8 Summary

This paper presented measurements of the substructure of jets containing prompt D^0 mesons and of inclusive jets in proton-proton collisions at $\sqrt{s} = 5.02$ TeV, in a data sample corresponding to an integrated luminosity of 301 pb^{-1} , collected in 2017 with the CMS experiment. The analysis focuses on the substructure of jets with transverse momentum $100 < p_T^{\text{jet}} < 120 \text{ GeV}$ and pseudorapidity $|\eta| < 1.6$, initially clustered with the anti- k_T algorithm and a distance parameter of $R = 0.2$. Both neutral and charged particles were used for the substructure of these jets. The D^0 mesons were identified via their two-pronged decays into a kaon and pion pair.

In this analysis, the opening angle between the subjet pair found using two different grooming algorithms based on Cambridge–Aachen reclustering was measured. The late- k_T algorithm consists of selecting the last splitting with a $k_T > 1 \text{ GeV}$ in the Cambridge–Aachen tree and gives access to hard, collinear emissions in an algorithmic way. The angular separation between the two hard subjets found with the soft-drop grooming algorithm was also studied, using the parameters $z_{\text{cut}} = 0.1$ and $\beta = 0$, with the additional requirement that the emission has a minimum relative transverse momentum of $k_T > 1 \text{ GeV}$. Measured angular distributions were compared to PYTHIA8 CP5 and HERWIG7 CH3 simulated events. HERWIG7 CH3 prediction describes angular distribution of inclusive jets better than PYTHIA8 CP5, while in case of jets containing prompt D^0 mesons both predictions fail to reproduce data. Dedicated PYTHIA8 CP5 and HERWIG7 CH3 predictions were produced to study impact of the gluon splitting to charm quark-antiquark pairs. The splitting angle distribution, in the case of soft-drop grooming algorithm, is sensitive to contributions from gluon splitting to charm quark-antiquark pairs at large angles. At the same time, the resulting angular distribution from late- k_T grooming algorithm is less sensitive to gluon splitting and to soft- and wide-angle radiation, and is more sensitive to the dead-cone effect. Although p_T^{jet} is much larger than the charm quark mass, it is possible to isolate hard collinear emissions and observe the suppression due to the charm quark mass in the hard and collinear region.

This is the first measurement of charm quark jet substructure that probes the hard and collinear region of the jet shower, therefore minimizing the hadronization effect and enabling a more direct connection with expected parton shower. The jet $p_T^{\text{jet}} > 100 \text{ GeV}$ selection, used for the first time for charm quark jet substructure, accesses the phase-space region which facilitates the interpretation of the jet substructure in terms of perturbative calculations. This measurement will serve as a reference for future studies in heavy ion collisions. In such interactions, the emissions induced by the strongly interacting quark-gluon plasma could be isolated in the region where vacuum emissions are vetoed by the dead cone.

Acknowledgments

We congratulate our colleagues in the CERN accelerator departments for the excellent performance of the LHC and thank the technical and administrative staffs at CERN and at other CMS institutes for their contributions to the success of the CMS effort. In addition, we gratefully acknowledge the computing centers and personnel of the Worldwide LHC Computing Grid and other centers for delivering so effectively the computing infrastructure essential to our analyses. Finally, we acknowledge the enduring support for the construction and operation of the LHC, the CMS detector, and the supporting computing infrastructure provided by the following funding agencies: SC (Armenia), BMBWF and FWF (Austria); FNRS and FWO (Belgium); CNPq, CAPES, FAPERJ, FAPERGS, and FAPESP (Brazil); MES and BNSF (Bulgaria); CERN; CAS, MoST, and NSFC (China); MINCIENCIAS (Colombia); MSES and CSF

(Croatia); RIF (Cyprus); SENESCYT (Ecuador); ERC PRG, RVTT3 and MoER TK202 (Estonia); Academy of Finland, MEC, and HIP (Finland); CEA and CNRS/IN2P3 (France); SRNSF (Georgia); BMBF, DFG, and HGF (Germany); GSRI (Greece); NKFIH (Hungary); DAE and DST (India); IPM (Iran); SFI (Ireland); INFN (Italy); MSIT and NRF (Republic of Korea); MES (Latvia); LMTLT (Lithuania); MOE and UM (Malaysia); BUAP, CINVESTAV, CONACYT, LNS, SEP, and UASLP-FAI (Mexico); MOS (Montenegro); MBIE (New Zealand); PAEC (Pakistan); MES and NSC (Poland); FCT (Portugal); MESTD (Serbia); MICIU/AEI and PCTI (Spain); MOSTR (Sri Lanka); Swiss Funding Agencies (Switzerland); MST (Taipei); MHESI and NSTDA (Thailand); TUBITAK and TENMAK (Türkiye); NASU (Ukraine); STFC (United Kingdom); DOE and NSF (USA).

Individuals have received support from the Marie-Curie program and the European Research Council and Horizon 2020 Grant, contract Nos. 675440, 724704, 752730, 758316, 765710, 824093, 101115353, 101002207, 101001205, and COST Action CA16108 (European Union); the Leventis Foundation; the Alfred P. Sloan Foundation; the Alexander von Humboldt Foundation; the Science Committee, project no. 22rl-037 (Armenia); the Fonds pour la Formation à la Recherche dans l'Industrie et dans l'Agriculture (FRIA-Belgium); the Beijing Municipal Science & Technology Commission, No. Z191100007219010, the Fundamental Research Funds for the Central Universities, the Ministry of Science and Technology of China under Grant No. 2023YFA1605804, and the Natural Science Foundation of China under Grant No. 12061141002 (China); the Ministry of Education, Youth and Sports (MEYS) of the Czech Republic; the Shota Rustaveli National Science Foundation, grant FR-22-985 (Georgia); the Deutsche Forschungsgemeinschaft (DFG), among others, under Germany's Excellence Strategy – EXC 2121 "Quantum Universe" – 390833306, and under project number 400140256 - GRK2497; the Hellenic Foundation for Research and Innovation (HFRI), Project Number 2288 (Greece); the Hungarian Academy of Sciences, the New National Excellence Program - ÚNKP, the NKFIH research grants K 131991, K 133046, K 138136, K 143460, K 143477, K 146913, K 146914, K 147048, 2020-2.2.1-ED-2021-00181, TKP2021-NKTA-64, and 2021-4.1.2-NEMZ_KI-2024-00036 (Hungary); the Council of Science and Industrial Research, India; ICSC – National Research Center for High Performance Computing, Big Data and Quantum Computing, FAIR – Future Artificial Intelligence Research, and CUP I53D23001070006 (Mission 4 Component 1), funded by the NextGenerationEU program (Italy); the Latvian Council of Science; the Ministry of Education and Science, project no. 2022/WK/14, and the National Science Center, contracts Opus 2021/41/B/ST2/01369 and 2021/43/B/ST2/01552 (Poland); the Fundação para a Ciência e a Tecnologia, grant CEECIND/01334/2018 (Portugal); the National Priorities Research Program by Qatar National Research Fund; MICIU/AEI/10.13039/501100011033, ERDF/EU, "European Union NextGenerationEU/PRTR", and Programa Severo Ochoa del Principado de Asturias (Spain); the Chulalongkorn Academic into Its 2nd Century Project Advancement Project, and the National Science, Research and Innovation Fund via the Program Management Unit for Human Resources & Institutional Development, Research and Innovation, grant B39G680009 (Thailand); the Kavli Foundation; the Nvidia Corporation; the SuperMicro Corporation; the Welch Foundation, contract C-1845; and the Weston Havens Foundation (USA).

References

- [1] Y. L. Dokshitzer, V. A. Khoze, A. H. Mueller, and S. I. Troian, "Basics of perturbative QCD". 1991.
- [2] ALICE Collaboration, "Direct observation of the dead cone effect in quantum chromodynamics", *Nature* **605** (2022) 440, doi:10.1038/s41586-022-04572-w,

- arXiv:2106.05713.
- [3] Y. L. Dokshitzer, V. A. Khoze, and S. I. Troian, “On specific QCD properties of heavy quark fragmentation (‘dead cone’),” *J. Phys. G* **17** (1991) 1602, doi:10.1088/0954-3899/17/10/023.
- [4] L. Cunqueiro, D. Napoletano, and A. Soto-Ontoso, “Dead cone searches in heavy-ion collisions using the jet tree”, *Phys. Rev. D* **107** (2023) 094008, doi:10.1103/PhysRevD.107.094008, arXiv:2211.11789.
- [5] CMS Collaboration, “Overview of high-density QCD studies with the CMS experiment at the LHC”, *Phys. Rept.* **1115** (2025) 219, doi:10.1016/j.physrep.2024.11.007, arXiv:2405.10785.
- [6] Y. L. Dokshitzer, G. D. Leder, S. Moretti, and B. R. Webber, “Better jet clustering algorithms”, *JHEP* **08** (1997) 001, doi:10.1088/1126-6708/1997/08/001, arXiv:hep-ph/9707323.
- [7] F. A. Dreyer, G. P. Salam, and G. Soyez, “The Lund Jet Plane”, *JHEP* **12** (2018) 064, doi:10.1007/JHEP12(2018)064, arXiv:1807.04758.
- [8] L. Cunqueiro and M. Płoskoń, “Searching for the dead cone effects with iterative declustering of heavy-flavor jets”, *Phys. Rev. D* **99** (2019) 074027, doi:10.1103/PhysRevD.99.074027, arXiv:1812.00102.
- [9] A. J. Larkoski, S. Marzani, G. Soyez, and J. Thaler, “Soft drop”, *JHEP* **05** (2014) 146, doi:10.1007/JHEP05(2014)146, arXiv:1402.2657.
- [10] J. M. Butterworth, A. R. Davison, M. Rubin, and G. P. Salam, “Jet substructure as a new Higgs search channel at the LHC”, *Phys. Rev. Lett.* **100** (2008) 242001, doi:10.1103/PhysRevLett.100.242001, arXiv:0802.2470.
- [11] ALICE Collaboration, “Measurements of groomed jet substructure of charm jets tagged by D^0 mesons in proton-proton collisions at $\sqrt{s} = 13 \text{ TeV}$ ”, *Phys. Rev. Lett.* **131** (2023) 192301, doi:10.1103/PhysRevLett.131.192301, arXiv:2208.04857.
- [12] CMS Collaboration, “Luminosity measurement in proton-proton collisions at 5.02 TeV in 2017 at CMS”, CMS Physics Analysis Summary CMS-PAS-LUM-19-001, 2021. <http://cds.cern.ch/record/2765655>.
- [13] “HEPData record for this analysis”, 2025. doi:10.17182/hepdata.156758.
- [14] CMS Collaboration, “The CMS experiment at the CERN LHC”, *JINST* **3** (2008) S08004, doi:10.1088/1748-0221/3/08/S08004.
- [15] CMS Collaboration, “Development of the CMS detector for the CERN LHC Run 3”, *JINST* **19** (2024) P05064, doi:10.1088/1748-0221/19/05/P05064, arXiv:2309.05466.
- [16] CMS Collaboration, “Performance of the CMS Level-1 trigger in proton-proton collisions at $\sqrt{s} = 13 \text{ TeV}$ ”, *JINST* **15** (2020) P10017, doi:10.1088/1748-0221/15/10/P10017, arXiv:2006.10165.
- [17] CMS Collaboration, “The CMS trigger system”, *JINST* **12** (2017) P01020, doi:10.1088/1748-0221/12/01/P01020, arXiv:1609.02366.

- [18] CMS Collaboration, “Electron and photon reconstruction and identification with the CMS experiment at the CERN LHC”, *JINST* **16** (2021) P05014, doi:10.1088/1748-0221/16/05/P05014, arXiv:2012.06888.
- [19] CMS Collaboration, “Performance of the CMS muon detector and muon reconstruction with proton-proton collisions at $\sqrt{s} = 13\text{ TeV}$ ”, *JINST* **13** (2018) P06015, doi:10.1088/1748-0221/13/06/P06015, arXiv:1804.04528.
- [20] CMS Collaboration, “Description and performance of track and primary-vertex reconstruction with the CMS tracker”, *JINST* **9** (2014) P10009, doi:10.1088/1748-0221/9/10/P10009, arXiv:1405.6569.
- [21] CMS Collaboration, “Particle-flow reconstruction and global event description with the CMS detector”, *JINST* **12** (2017) P10003, doi:10.1088/1748-0221/12/10/P10003, arXiv:1706.04965.
- [22] CMS Collaboration, “Performance of reconstruction and identification of τ leptons decaying to hadrons and ν_τ in pp collisions at $\sqrt{s} = 13\text{ TeV}$ ”, *JINST* **13** (2018) P10005, doi:10.1088/1748-0221/13/10/P10005, arXiv:1809.02816.
- [23] CMS Collaboration, “Jet energy scale and resolution in the CMS experiment in pp collisions at 8 TeV”, *JINST* **12** (2017) P02014, doi:10.1088/1748-0221/12/02/P02014, arXiv:1607.03663.
- [24] CMS Collaboration, “Performance of missing transverse momentum reconstruction in proton-proton collisions at $\sqrt{s} = 13\text{ TeV}$ using the CMS detector”, *JINST* **14** (2019) P07004, doi:10.1088/1748-0221/14/07/P07004, arXiv:1903.06078.
- [25] T. Sjöstrand et al., “An introduction to PYTHIA8.2”, *Comput. Phys. Commun.* **191** (2015) 159, doi:10.1016/j.cpc.2015.01.024, arXiv:1410.3012.
- [26] CMS Collaboration, “Extraction and validation of a new set of CMS PYTHIA8 tunes from underlying event measurements”, *Eur. Phys. J. C* **80** (2020) 4, doi:10.1140/epjc/s10052-019-7499-4, arXiv:1903.12179.
- [27] S. Gieseke, P. Stephens, and B. Webber, “New formalism for QCD parton showers”, *JHEP* **12** (2003) 045, doi:10.1088/1126-6708/2003/12/045, arXiv:hep-ph/0310083.
- [28] NNPDF Collaboration, “Parton distributions for the LHC Run 2”, *JHEP* **04** (2015) 040, doi:10.1007/JHEP04(2015)040, arXiv:1410.8849.
- [29] B. R. Webber, “A QCD model for jet fragmentation including soft gluon interference”, *Nucl. Phys. B* **238** (1984) 492, doi:10.1016/0550-3213(84)90333-X.
- [30] CMS Collaboration, “Development and validation of HERWIG7 tunes from CMS underlying event measurements”, *Eur. Phys. J. C* **81** (2021) 312, doi:10.1140/epjc/s10052-021-08949-5, arXiv:2011.03422.
- [31] GEANT4 Collaboration, “GEANT4—a simulation toolkit”, *Nucl. Instrum. Meth. A* **506** (2003) 250, doi:10.1016/S0168-9002(03)01368-8.
- [32] P. Skands, S. Carrazza, and J. Rojo, “Tuning PYTHIA8.1: the Monash 2013 tune”, *Eur. Phys. J. C* **74** (2014) 3024, doi:10.1140/epjc/s10052-014-3024-y, arXiv:1404.5630.

- [33] CMS Collaboration, “Event generator tunes obtained from underlying event and multiparton scattering measurements”, *Eur. Phys. J. C* **76** (2016) 155, doi:10.1140/epjc/s10052-016-3988-x, arXiv:1512.00815.
- [34] M. Cacciari, G. P. Salam, and G. Soyez, “The anti- k_T jet clustering algorithm”, *JHEP* **04** (2008) 063, doi:10.1088/1126-6708/2008/04/063, arXiv:0802.1189.
- [35] M. Cacciari, G. P. Salam, and G. Soyez, “FastJet user manual”, *Eur. Phys. J. C* **72** (2012) 1896, doi:10.1140/epjc/s10052-012-1896-2, arXiv:1111.6097.
- [36] H. A. Andrews et al., “Novel tools and observables for jet physics in heavy-ion collisions”, *J. Phys. G* **47** (2020) 065102, doi:10.1088/1361-6471/ab7cbc, arXiv:1808.03689.
- [37] CMS Collaboration, “Determination of jet energy calibration and transverse momentum resolution in CMS”, *JINST* **6** (2011) P11002, doi:10.1088/1748-0221/6/11/P11002, arXiv:1107.4277.
- [38] Particle Data Group, S. Navas et al., “Review of particle physics”, *Phys. Rev. D* **110** (2024) 030001, doi:10.1103/PhysRevD.110.030001.
- [39] H. Voss, A. Höcker, J. Stelzer, and F. Tegenfeldt, “TMVA, the toolkit for multivariate data analysis with ROOT”, in *Proc. XIth International Workshop on Advanced Computing and Analysis Techniques in Physics Research (ACAT)*, p. 40. 2007. arXiv:physics/0703039. doi:10.22323/1.050.0040.
- [40] CMS Collaboration, “Studies of charm quark diffusion inside jets using PbPb and pp collisions at $\sqrt{s_{\text{NN}}} = 5.02 \text{ TeV}$ ”, *Phys. Rev. Lett.* **125** (2020) 102001, doi:10.1103/PhysRevLett.125.102001, arXiv:1911.01461.
- [41] M. Wobisch and T. Wengler, “Hadronization corrections to jet cross sections in deep inelastic scattering”, in *Proc. Workshop on Monte Carlo generators for HERA physics*, p. 270. 1998. arXiv:hep-ph/9907280. doi:10.48550/arXiv.hep-ph/9907280.
- [42] S. Caletti, A. Ghira, and S. Marzani, “On heavy-flavor jets with soft drop”, *Eur. Phys. J. C* **84** (2024) 212, doi:10.1140/epjc/s10052-024-12562-7, arXiv:2312.11623.
- [43] G. D’Agostini, “A multidimensional unfolding method based on Bayes’ theorem”, *Nucl. Instrum. Meth. A* **362** (1995) 487, doi:10.1016/0168-9002(95)00274-X.
- [44] T. Adye, “Unfolding algorithms and tests using RooUnfold”, in *Proc. PHYSTAT 2011 Workshop on Statistical Issues Related to Discovery Claims in Search Experiments and Unfolding*, H. Prosper and L. Lyons, eds., p. 313. Geneva, Switzerland, 2011. arXiv:1105.1160. doi:10.5170/CERN-2011-006.313.
- [45] CMS Collaboration, “Single-particle response in the CMS calorimeters”, CMS Physics Analysis Summary CMS-PAS-JME-10-008, 2010.
- [46] CMS Collaboration, “Measurements of azimuthal anisotropy of nonprompt D^0 mesons in PbPb collisions at 5.02TeV”, *Phys. Lett. B* **850** (2024) 138389, doi:10.1016/j.physletb.2023.138389, arXiv:2212.01636.
- [47] CMS Collaboration, “Study of quark and gluon jet substructure in Z+jet and dijet events from pp collisions”, *JHEP* **01** (2022) 188, doi:10.1007/JHEP01(2022)188, arXiv:2109.03340.

- [48] CMS Collaboration, “Measurement of the primary Lund jet plane density in proton-proton collisions at $\sqrt{s} = 13$ TeV”, *JHEP* **05** (2024) 116,
doi:10.1007/JHEP05(2024)116, arXiv:2312.16343.

- ³⁸Also at University of Visva-Bharati, Santiniketan, India
³⁹Also at Indian Institute of Science (IISc), Bangalore, India
⁴⁰Also at Amity University Uttar Pradesh, Noida, India
⁴¹Also at UPES - University of Petroleum and Energy Studies, Dehradun, India
⁴²Also at IIT Bhubaneswar, Bhubaneswar, India
⁴³Also at Institute of Physics, Bhubaneswar, India
⁴⁴Also at University of Hyderabad, Hyderabad, India
⁴⁵Also at Deutsches Elektronen-Synchrotron, Hamburg, Germany
⁴⁶Also at Isfahan University of Technology, Isfahan, Iran
⁴⁷Also at Sharif University of Technology, Tehran, Iran
⁴⁸Also at Department of Physics, University of Science and Technology of Mazandaran, Behshahr, Iran
⁴⁹Also at Department of Physics, Faculty of Science, Arak University, ARAK, Iran
⁵⁰Also at Italian National Agency for New Technologies, Energy and Sustainable Economic Development, Bologna, Italy
⁵¹Also at Centro Siciliano di Fisica Nucleare e di Struttura Della Materia, Catania, Italy
⁵²Also at Università degli Studi Guglielmo Marconi, Roma, Italy
⁵³Also at Scuola Superiore Meridionale, Università di Napoli 'Federico II', Napoli, Italy
⁵⁴Also at Fermi National Accelerator Laboratory, Batavia, Illinois, USA
⁵⁵Also at Lulea University of Technology, Lulea, Sweden
⁵⁶Also at Consiglio Nazionale delle Ricerche - Istituto Officina dei Materiali, Perugia, Italy
⁵⁷Also at Institut de Physique des 2 Infinis de Lyon (IP2I), Villeurbanne, France
⁵⁸Also at Department of Applied Physics, Faculty of Science and Technology, Universiti Kebangsaan Malaysia, Bangi, Malaysia
⁵⁹Also at Consejo Nacional de Ciencia y Tecnología, Mexico City, Mexico
⁶⁰Also at INFN Sezione di Torino, Università di Torino, Torino, Italy; Università del Piemonte Orientale, Novara, Italy
⁶¹Also at Trincomalee Campus, Eastern University, Sri Lanka, Nilaveli, Sri Lanka
⁶²Also at Saegis Campus, Nugegoda, Sri Lanka
⁶³Also at National and Kapodistrian University of Athens, Athens, Greece
⁶⁴Also at Ecole Polytechnique Fédérale Lausanne, Lausanne, Switzerland
⁶⁵Also at Universität Zürich, Zurich, Switzerland
⁶⁶Also at Stefan Meyer Institute for Subatomic Physics, Vienna, Austria
⁶⁷Also at Laboratoire d'Annecy-le-Vieux de Physique des Particules, IN2P3-CNRS, Annecy-le-Vieux, France
⁶⁸Also at Near East University, Research Center of Experimental Health Science, Mersin, Turkey
⁶⁹Also at Konya Technical University, Konya, Turkey
⁷⁰Also at Izmir Bakircay University, Izmir, Turkey
⁷¹Also at Adiyaman University, Adiyaman, Turkey
⁷²Also at Bozok Universitetesi Rektörlüğü, Yozgat, Turkey
⁷³Also at Marmara University, Istanbul, Turkey
⁷⁴Also at Milli Savunma University, Istanbul, Turkey
⁷⁵Also at Kafkas University, Kars, Turkey
⁷⁶Now at Istanbul Okan University, Istanbul, Turkey
⁷⁷Also at Hacettepe University, Ankara, Turkey
⁷⁸Also at Erzincan Binali Yıldırım University, Erzincan, Turkey
⁷⁹Also at Istanbul University - Cerrahpasa, Faculty of Engineering, Istanbul, Turkey
⁸⁰Also at Yildiz Technical University, Istanbul, Turkey

⁸¹Also at School of Physics and Astronomy, University of Southampton, Southampton, United Kingdom

⁸²Also at Monash University, Faculty of Science, Clayton, Australia

⁸³Also at Università di Torino, Torino, Italy

⁸⁴Also at Bethel University, St. Paul, Minnesota, USA

⁸⁵Also at Karamanoğlu Mehmetbey University, Karaman, Turkey

⁸⁶Also at California Institute of Technology, Pasadena, California, USA

⁸⁷Also at United States Naval Academy, Annapolis, Maryland, USA

⁸⁸Also at Ain Shams University, Cairo, Egypt

⁸⁹Also at Bingol University, Bingol, Turkey

⁹⁰Also at Georgian Technical University, Tbilisi, Georgia

⁹¹Also at Sinop University, Sinop, Turkey

⁹²Also at Erciyes University, Kayseri, Turkey

⁹³Also at Horia Hulubei National Institute of Physics and Nuclear Engineering (IFIN-HH), Bucharest, Romania

⁹⁴Now at another institute formerly covered by a cooperation agreement with CERN

⁹⁵Also at Texas A&M University at Qatar, Doha, Qatar

⁹⁶Also at another institute formerly covered by a cooperation agreement with CERN

⁹⁷Also at Yerevan Physics Institute, Yerevan, Armenia

⁹⁸Also at Imperial College, London, United Kingdom

⁹⁹Also at Institute of Nuclear Physics of the Uzbekistan Academy of Sciences, Tashkent, Uzbekistan